Optimized Control Set Model Predictive Control for Dual Three-Phase PMSM With Minimum Error Duty Cycle Regulation

Jia Cui, Tao Tao, and Wenxiang Zhao, *Senior Member, IEEE*

***Abstract*—The conventional model predictive control for dual three-phase permanent magnet synchronous motor suffers from poor operational performance and heavy computational burdens. Aiming to solve the two problems, this article proposes an optimized control set model predictive control with a minimum error duty cycle strategy. First, a new form of 24 virtual voltage vector control set is constructed. All voltage vectors in the new control set are pointed in different directions and distributed uniformly, which are facilitated by combining with duty cycle modulation techniques. The control precision can be enhanced by employing the new control with more candidate vectors. Furthermore, a minimum error duty cycle calculation method is proposed in the scheme, where the currents of the *dq*-axis are considered simultaneously even if one active voltage vector is employed. So, the errors between the reference voltage and the selected voltage vector can be reduced. Thus, the operational performance can be significantly improved. Especially, a multistage group evaluation method is proposed to simplify the enumeration process, which guarantees that the proposed strategy can evaluate more vectors with less computational burden. Comprehensive experiments are carried out to verify the effectiveness of the proposed method.**

***Index Terms*—Computational burden, dual three-phase permanent synchronous magnet motor, minimum error duty cycle, model predictive control (MPC), optimized control set.**

NOMENCLATURE

R_s	Stator winding resistance.
ω_e	Electrical rotor speed.
ψ_f	Flux of rotor permanent magnet.
L_d, L_q	*dq*-axis inductances.
n_p	Number of pole pairs.
T_s	Control period.
$\mathrm{U_{dc}}$	DC bus voltage.
i_d^* i_q^*	*dq*-axis reference currents.
i_d^k, i_q^k, i_x^k, i_y^k	*dq*- and *xy*-axis currents at *k* instant.
i_d^{k+i}, i_q^{k+i}, i_x^{k+i}, i_y^{k+i}	*dq*- and *xy*-axis currents at $k+i$ instant.
u_d^k, u_q^k, u_x^k, u_y^k	*dq*- and *xy*-axis voltages at *k* instant.
$\boldsymbol{u}_i$	Basic voltage vectors.
$\boldsymbol{u}_i^\alpha$, $\boldsymbol{u}_i^\beta$, $\boldsymbol{u}_i^x$, $\boldsymbol{u}_i^y$	$\alpha\beta$- and *xy*-subspace voltage vectors.
$\mathbf{V}_i$	Virtual voltage vectors, (i = 1,2,3, …,24).
$\mathbf{V}_{\mathrm{obj}}$	Objective virtual voltage vector.
$\mathbf{V}_{\mathrm{obj}}^\alpha$, $\mathbf{V}_{\mathrm{obj}}^\beta$, $\mathbf{V}_{\mathrm{obj}}^x$, $\mathbf{V}_{\mathrm{obj}}^y$	$\alpha\beta$- and *xy*-axis components of $\mathbf{V}_{\mathrm{obj}}$.
$\boldsymbol{u}_{L_1}^{\alpha\beta}$, $\boldsymbol{u}_{L_3}^{\alpha\beta}$, $\boldsymbol{u}_{L_4}^{\alpha\beta}$	$\alpha\beta$-axis components of basic voltage vector in L_1, L_3, and L_4 groups.
$\boldsymbol{u}_{L_1}^{xy}$, $\boldsymbol{u}_{L_3}^{xy}$, $\boldsymbol{u}_{L_4}^{xy}$	*xy*-axis components of basic voltage vector in L_1, L_3, and L_4 groups.

Manuscript received 16 February 2023; revised 7 August 2023; accepted 30 September 2023. Date of publication 13 October 2023; date of current version 6 December 2023. This work was supported by the National Natural Science Foundation of China under Grants 52025073 and 52107047. Recommended for publication by Associate Editor F. Khan. *(Corresponding author: Tao Tao.)*

Jia Cui is with the School of Electrical and Information Engineering, Jiangsu University, Zhenjiang 212013, China, and also with the College of Automation, Jiangsu University of Science and Technology, Zhenjiang 212013, China (e-mail: cuijia1030@qq.com).

Tao Tao is with the School of Electrical and Information Engineering, Jiangsu University, Zhenjiang 212013, China (e-mail: taotao0511@ujs.edu.cn).

Wenxiang Zhao is with the School of Electric Power Engineering, Nanjing Institute of Technology, Nanjing 211100, China, and also with the School of Electrical and Information Engineering, Jiangsu University, Zhenjiang 212013, China (e-mail: zwx@ujs.edu.cn).

Color versions of one or more figures in this article are available at https://doi.org/10.1109/TPEL.2023.3324209.

Digital Object Identifier 10.1109/TPEL.2023.3324209

I. INTRODUCTION

COMPARED with conventional three-phase motors, multiphase motors have received great attention from the power electronics field due to their congenital advantages of high efficiency, high power density, and good fault-tolerant capability [1], [2]. In recent decades, they have been extensively applied to high-performance industries, such as aerospace, ship propulsion, and renewable vehicles. As a representative of multi-three-phase motors, the dual three-phase permanent magnet synchronous motor (DTP-PMSM) can eliminate 6*k*-order torque ripples, owing to the special structure, where two sets of three-phase stator windings spatially shifted by 30 electrical degrees [3], [4], [5], [6]. Also, the majority control strategy of the conventional three-phase motor can be extended to the DTP-PMSM easily.

Over the years, the control of DTP-PMSMs has been discussed by many scholars. The field-oriented control (FOC) was introduced in [7], where the space vector pulsewidth modulation (PWM) strategy was adopted. In the FOC, four adjacent voltage vectors and one zero vector were selected to participate in modulation, and an excellent steady-state performance could be obtained. However, the FOC has the drawbacks of complex parameter adjustment and weak dynamic response. As a new prominent control method in motor control, the finite-control-set model predictive control (denoted as MPC for brevity) is a prominent strategy in handling multivariable control and nonlinear constraints [8], [9], [10]. In [11], the MPC was used

for a dual three-phase induction motor to overcome the difficulties of multiphase current control and to avoid a complex modulation process. The current components in $\alpha\beta$-subspace and *xy*-subspace were considered in the cost function. However, the method of constraining the components in *xy*-subspace by weight coefficients was inaccurate. In order to suppress the current harmonics in the *xy*-subspace, the virtual vector (VV) technique was proposed in [12], [13], and [14]. The classical VV used multiple basic voltage vectors to synthesize a harmonic-free vector, where the harmonic currents and torque ripple were well weakened in the multiphase drive system [15], [16]. In addition, the control set consists of 64 basic voltage vectors since the dual three-phase motors are fed by a two-level six-phase voltage-source inverter. There is challenging work to evaluate all the voltage vectors to select the optimal one. The VV method of the DTP-PMSM drive system contains 12 harmonic-free voltage vectors, which can reduce computation time and improve operational performance [17], [18].

The dominant characteristic of the MPC lies in the intuitive concept. However, the steady-state performance is restricted by the limited numbers of voltage vectors in the conventional MPC. Hence, several methods were proposed to improve the steady-state performance of the MPC. The extended control set method was designed in [19], [20], and [21], where more vectors were included in the control set. However, the complexity of the algorithm increases significantly with more and more voltage vectors involved. Especially in a multiphase MPC system, the candidate vectors increased exponentially with the motor phase increase. In order to avoid this time-consuming work, a series of simplification works were investigated in [22], [23], and [24]. Combining the ideas of direct torque control and MPC, the torque and flux observers were designed to preselect three qualified voltage vectors in the control set. Although this approach reduced computation, two more observers complicated the control structure. Tao et al. [25] divided the control set into main and auxiliary parts and evaluated each part step-by-step. This method retained the simple scheme of the MPC and reduced the computational burden. However, the method will be inefficient when more voltage vectors are included in the control set. Another way to improve system performance is to change the topology. In [26], [27], and [28], multilevel inverters were introduced in MPC for low output voltages and current harmonics. Considering the online calculation and vector selection, complex computation seems unavoidable for the practical implementation of the MPC. The execution time becomes significantly longer with the increasing complexity of power converters and the number of switching states. Also, the multilevel inverters will increase the cost. Moreover, the duty cycle modulation technique is introduced to the MPC scheme to improve operational performance. In [29], a null vector and the selected active voltage vector were inserted in one control period to achieve torque ripple reduction. However, this method cannot offer satisfactory performance due to the calculation errors of the duty cycle. To cope with this problem, some variants of MPC were proposed in [30], [31], and [32], where three vectors (two active vectors and one null vector) were used in one period. However, this online space vector modulation approach generates a sizeable computational pressure.

This article proposes a new control set with a minimum error duty cycle calculation method. The proposed method presents better performance without increasing the computational burden. The main contributions of this article are as follows.

1) A control set with 24 VVs is designed according to the modulation theory. The designed control set has a denser voltage vector distribution, presenting a smaller torque variation slope during the voltage vector switching procedure.
2) A novel duty cycle calculation method is proposed according to the geometric relationship between the reference and the predicted current. When only the single VV is considered, this method can obtain the duty cycle with the smallest error.
3) A multistage group evaluation method is proposed to simplify the evaluation process, alleviating the computational burden and improving execution efficiency.
4) The proposed and existing methods are compared experimentally from the aspects of steady state, dynamic state, and parameter variation.

The rest of this article is organized as follows. Section II introduces the form of the conventional 24 VV method. Section III elaborates on the process of the proposed method. Experiments are designed to verify the proposed method in Section IV. Finally, Section V concludes this article.

II. Conventional 24 Virtual Voltage Vectors

The six-phase two-level voltage-source inverter is applied to drive the DTP-PMSM. Each bridge leg can present two states (OFF and ON) since the complementary state of two switching devices is in the same bridge legs. Thus, there are $2^6 = 64$ switching combinations. The corresponding voltage vector number is defined as $i = S_A S_B S_C\text{-}S_D S_E S_F$, where S_j ($j = A, B, C, D, E, F$) represents the switching state of the upper legs (ON is "1," while OFF is "0"). The i is converted to an octal number to facilitate recording. For example, 13 represents "001-011." The 64 voltage vectors in the $\alpha\beta$-subspace and *xy*-subspace can be obtained by using

$$\begin{cases} \boldsymbol{u}_{\alpha\beta} = U_{\mathrm{dc}}(S_A + S_B a^4 + S_C a^8 + S_D a + S_E a^5 + S_F a^9)/3 \\ \boldsymbol{u}_{xy} = U_{\mathrm{dc}}(S_A + S_B a^8 + S_C a^4 + S_D a^5 + S_E a + S_F a^9)/3 \end{cases} \tag{1}$$

where $a = \exp(j30°)$.

Fig. 1 shows the distributions of the voltage vectors in different subspaces where the zero voltage vectors are neglected. The 60 active vectors in $\alpha\beta$-subspace can be divided into four dodecagons with different magnitudes, from innermost to outermost, named, $L_1(0.173U_{\mathrm{dc}})$, $L_2(0.333U_{\mathrm{dc}})$, $L_3(0.471U_{\mathrm{dc}})$, and $L_4(0.644U_{\mathrm{dc}})$, respectively.

It should be noted in Fig. 1 that the outermost vectors in $\alpha\beta$-subspace are mapped into the innermost in *xy*-subspace, while the innermost vectors in $\alpha\beta$-subspace are mapped into the outermost in *xy*-subspace. However, the two middle group vectors in $\alpha\beta$-subspace still mapped into the *xy*-subspace with

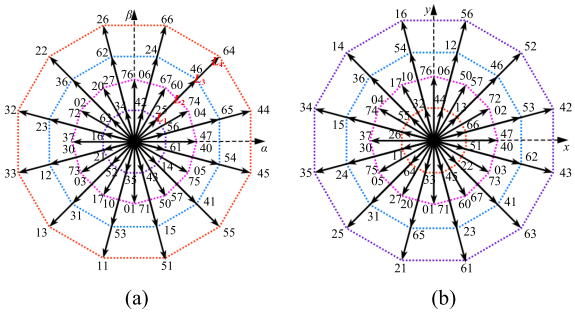

Fig. 1. Distributions of the voltage vectors in different subspaces. (a) $\alpha\beta$-subspace. (b) *xy*-subspace.

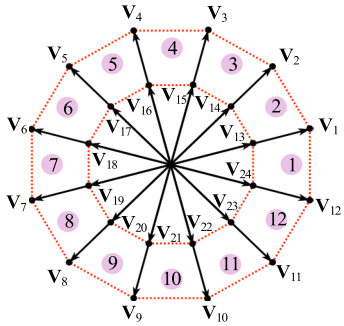

Fig. 2. Distributions of classical 24 VVs.

the same magnitude. In addition, some vectors in dodecagons L_1, L_3, and L_4 point to the same direction in $\alpha\beta$-subspace, whereas the vectors in L_3 have the opposite direction with L_1 and L_4 in *xy*-subspace. Consequently, the harmonic-free vectors can be synthesized by allocating the proportion for the two basic vectors in L_4 and L_3 groups or L_1 and L_3 groups.

According to the definition of harmonic-free vectors, the sum of projections on the *xy*-subspace is zero. Thus, the relationship for the basic vectors in L_4 and L_3 groups can be expressed as

$$\begin{cases} D_{L_4}^{34} \cdot \left|\boldsymbol{u}_{L_4}^{xy}\right| - D_{L_3}^{34} \cdot \left|\boldsymbol{u}_{L_3}^{xy}\right| = 0 \\ D_{L_4}^{34} + D_{L_3}^{34} = 1 \end{cases} \tag{2}$$

where $D_{L_3}^{34}$ and $D_{L_4}^{34}$ represent the duty cycles of basic vector in L_3 and L_4 groups when the L_3 and L_4 are used to synthesize VV.

Another synthesis method can be expressed as (3) since the basic vectors belong to L_1 and L_3 groups

$$\begin{cases} D_{L_1}^{13} \cdot \left|\boldsymbol{u}_{L_1}^{xy}\right| - D_{L_3}^{13} \cdot \left|\boldsymbol{u}_{L_3}^{xy}\right| = 0 \\ D_{L_1}^{13} + D_{L_3}^{13} = 1 \end{cases} \tag{3}$$

where $D_{L_1}^{13}$ and $D_{L_3}^{13}$ represent the duty cycles of basic vector in L_1 and L_3 groups when the L_1 and L_3 are used to synthesize VV.

By substituting the magnitude of L_1, L_3, and L_4 in harmonic subspace ($\left|\boldsymbol{u}_{L_1}^{xy}\right| = 0.173U_{\mathrm{dc}}$, $\left|\boldsymbol{u}_{L_3}^{xy}\right| = 0.471U_{\mathrm{dc}}$, and $\left|\boldsymbol{u}_{L_4}^{xy}\right| = 0.644U_{\mathrm{dc}}$) into (2) and (3), the proportion can be obtained as

$$\begin{cases} D_{L_3}^{34} = 0.268 \\ D_{L_4}^{34} = 0.732 \end{cases}, \quad \begin{cases} D_{L_1}^{13} = 0.423 \\ D_{L_3}^{13} = 0.577. \end{cases} \tag{4}$$

The magnitude of the synthesized vector can be expressed as

$$M_{34} = D_{L_3}^{34} \cdot \left|\boldsymbol{u}_{L_3}^{\alpha\beta}\right| + D_{L_4}^{34} \cdot \left|\boldsymbol{u}_{L_4}^{\alpha\beta}\right| = 0.597U_{\mathrm{dc}} \tag{5}$$

$$M_{13} = D_{L_1}^{13} \cdot \left|\boldsymbol{u}_{L_1}^{\alpha\beta}\right| + D_{L_3}^{13} \cdot \left|\boldsymbol{u}_{L_3}^{\alpha\beta}\right| = 0.345U_{\mathrm{dc}}. \tag{6}$$

Based on this analysis, two sets of VVs with different magnitudes are synthesized, which confirms the effectiveness of reducing the harmonic currents [19]. The distributions of classical VVs are shown in Fig. 2. There are 24 VVs on the distribution map. The magnitude of the outer layer VVs is $0.597U_{\mathrm{dc}}$, and the magnitude of the inner layer VVs is $0.345U_{\mathrm{dc}}$. The synthetic principle can be summarized as

$$\begin{cases} \mathbf{V}_{\mathrm{outer}} = 0.268 \times \boldsymbol{u}_{L_3} + 0.732 \times \boldsymbol{u}_{L_4} \\ \mathbf{V}_{\mathrm{inner}} = 0.577 \times \boldsymbol{u}_{L_3} + 0.423 \times \boldsymbol{u}_{L_1}. \end{cases} \tag{7}$$

III. Proposed 24 Virtual Voltage Vectors and Predictive Duty Cycle Control

The classical 24-VV method in the DTP-PMSM drive system consists of 12 large VVs and 12 small VVs. However, the small VV can be replaced ($\mathbf{V}_{\mathrm{inner}} = 0.578\mathbf{V}_{\mathrm{outer}}$) by the large VVs since the duty cycle modulation method is employed. It increases the computational burden and is useless for performance improvement. In this section, a new form 24-VV control set is designed, where the duty cycle modulation technique can fully utilize all VVs.

A. Reconstructed 24 Virtual Voltage Vectors

It can be seen from Fig. 2 that the $\alpha\beta$-subspace is divided into 12 sectors uniformly, and the angle between the adjacent two vectors is 30°. However, the modulation region is limited to the vertices of the regular dodecagon, resulting in insufficient control precision. Therefore, this section reconstructed 24 VVs with equal magnitude and even phase angle, presenting a wider modulation region than the classical 24-VV method.

There are several basic voltage vectors utilized to synthesize one VV. The sum of all voltage vectors in the harmonic subspace components is equal to zero. The principle can be expressed as

$$\begin{cases} \sum_{i=1}^{n} D_i \boldsymbol{u}_i^x = \sum_{i=1}^{n} D_i \boldsymbol{u}_i^y = 0 \\ \sum_{i=1}^{n} D_i = 1 \end{cases} \tag{8}$$

where D_i represents the duty cycle of the basic voltage vector.

In the motor control field, the voltage utilization is related to the magnitude of the voltage vector [18]. According to the mathematical theory, the larger the magnitude of the basic vector involved in the synthesis process, the larger the magnitude of the new vector that can be synthesized. In order to obtain higher voltage utilization, the adjacent three voltage vectors in the L_4 group are adopted in the proposed method. Fig. 3 shows the schematic diagram of the proposed VVs. According to the geometric relations of the synthesis principle, the component of $\mathbf{V}_{\mathrm{obj}}$ in the $\alpha\beta$-axis equals the sum of the components of $\boldsymbol{u}_{66}$,

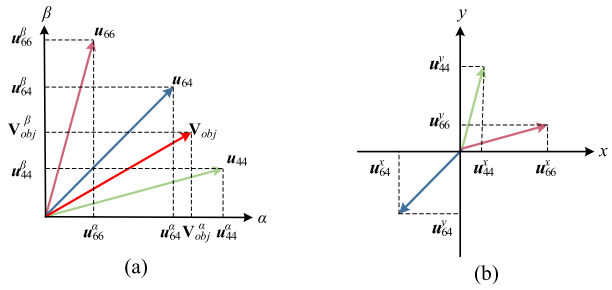

Fig. 3. Composition diagram of $\mathbf{V}_{\mathrm{obj}}$. (a) $\alpha\beta$-subspace. (b) xy-subspace.

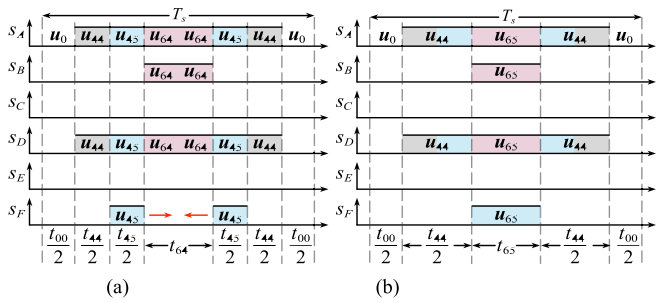

Fig. 4. Switch pattern of $\mathbf{V}_{\mathrm{obj}}$. (a) Expected. (b) Generated.

$\boldsymbol{u}_{64}$, and $\boldsymbol{u}_{44}$, whereas the harmonic components equal zero. The equation can be described as

$$\begin{cases} D_1 \cdot \boldsymbol{u}_{66}^{\alpha} + D_2 \cdot \boldsymbol{u}_{64}^{\alpha} + D_3 \cdot \boldsymbol{u}_{44}^{\alpha} = \mathbf{V}_{\mathrm{obj}}^{\alpha} \\ D_1 \cdot \boldsymbol{u}_{66}^{\beta} + D_2 \cdot \boldsymbol{u}_{64}^{\beta} + D_3 \cdot \boldsymbol{u}_{44}^{\beta} = \mathbf{V}_{\mathrm{obj}}^{\beta} \\ D_1 \cdot \boldsymbol{u}_{66}^{x} + D_2 \cdot \boldsymbol{u}_{64}^{x} + D_3 \cdot \boldsymbol{u}_{44}^{x} = \mathbf{V}_{\mathrm{obj}}^{x} = 0 \\ D_1 \cdot \boldsymbol{u}_{66}^{y} + D_2 \cdot \boldsymbol{u}_{64}^{y} + D_3 \cdot \boldsymbol{u}_{44}^{y} = \mathbf{V}_{\mathrm{obj}}^{y} = 0. \end{cases} \tag{9}$$

In addition, the isosceles triangular wave is used as a carrier wave in the practical digital signal processor (DSP) system. The high level in the standard switching pattern will be concentrated in the central position. Also, the switch of each phase does not operate more than once in one period. Since the VV technique employed multiple basic vectors, several expected synthesized processes in this carrier mode are inconsistent with the generated vector. The synthesis principle needs to be adjusted for the VV at a specific location.

For example, when the angle between the $\mathbf{V}_{\mathrm{obj}}$ and α-axis is 15°, the adjacent three vectors are $\boldsymbol{u}_{44}$, $\boldsymbol{u}_{45}$, and $\boldsymbol{u}_{64}$, respectively. The switching pattern of $\mathbf{V}_{\mathrm{obj}}$ synthesized by $\boldsymbol{u}_{44}$, $\boldsymbol{u}_{45}$, and $\boldsymbol{u}_{64}$ is depicted in Fig. 4(a), as can be seen from Fig. 4(a), in which the S_F acts two times in one period. Therefore, the high level of the F-phase will be concentrated in the central position. The new switching pattern transforms the basic voltage vectors to $\boldsymbol{u}_{44}$ and $\boldsymbol{u}_{65}$. The composition diagram of this synthesis method is shown in Fig. 5, where two equidirectional vectors in L_4 and L_3 groups are actually selected to synthesize the VV. According to the above analysis, it is found that the VVs at 15°, 75°, 135°, 195°, 255°, and 315° all conform to this rule. Hence, when these VVs are involved, only two basic active voltage vectors are selected to participate in the calculation.

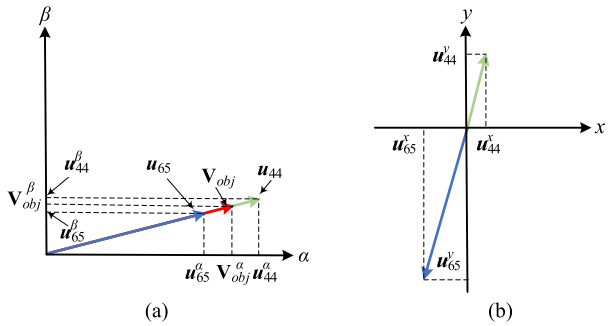

Fig. 5. Composition diagram of $\mathbf{V}_{\mathrm{obj}}$ when the VV is located at 15°. (a) $\alpha\beta$-subspace. (b) xy-subspace.

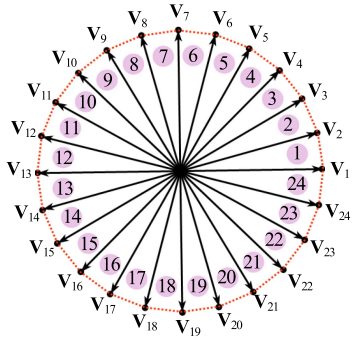

Fig. 6. Distributions of proposed 24 VVs.

The final synthesis principle can be expressed as

$$\begin{bmatrix} \mathbf{V}_i^{\alpha} \\ \mathbf{V}_i^{\beta} \\ \mathbf{V}_i^{x} \\ \mathbf{V}_i^{y} \\ 1 \end{bmatrix} = \begin{bmatrix} \boldsymbol{u}_{1\mathrm{st}}^{\alpha} & \boldsymbol{u}_{2\mathrm{nd}}^{\alpha} & \boldsymbol{u}_{3\mathrm{rd}}^{\alpha} & 0 \\ \boldsymbol{u}_{1\mathrm{st}}^{\beta} & \boldsymbol{u}_{2\mathrm{nd}}^{\beta} & \boldsymbol{u}_{3\mathrm{rd}}^{\beta} & 0 \\ \boldsymbol{u}_{1\mathrm{st}}^{x} & \boldsymbol{u}_{2\mathrm{nd}}^{x} & \boldsymbol{u}_{3\mathrm{rd}}^{x} & 0 \\ \boldsymbol{u}_{1\mathrm{st}}^{y} & \boldsymbol{u}_{2\mathrm{nd}}^{y} & \boldsymbol{u}_{3\mathrm{rd}}^{y} & 0 \\ 1 & 1 & 1 & 1 \end{bmatrix} \begin{bmatrix} D_1 \\ D_2 \\ D_3 \\ D_0 \end{bmatrix} \tag{10}$$

where $\boldsymbol{u}_{1\mathrm{st}}$, $\boldsymbol{u}_{2\mathrm{nd}}$, and $\boldsymbol{u}_{3\mathrm{rd}}$ represent the first, second, and third primary vectors, respectively. The $\boldsymbol{u}_{3\mathrm{rd}}$ and D_3 equal zero when two equidirectional vectors are used to synthesize the VVs.

It should be noted that (10) has no guaranteed trivial solutions due to three variables but four equations. Hence, more constraints are needed to solve the ratio of each basic vector. The detailed solution is divided into the following steps.

First, the distribution of 24 VVs to be synthesized is shown in Fig. 6, where the $\alpha\beta$-subspace is divided into 24 sectors uniformly, and the angle between adjacent vectors is 15°. The position of each vector is determined while the magnitude is not calculated. In addition, the ratio of each vector must be greater than or equal to zero. The constraints can be expressed as

$$\begin{cases} 0 \le D_1 \le 1 \\ 0 \le D_2 \le 1 \\ 0 \le D_3 \le 1 \\ 0 \le D_4 \le 1. \end{cases} \tag{11}$$

Assuming the magnitudes of 24 VVs are equal. Equations (10) and (11) constitute the conditional equations. Therefore, the magnitude can be set from small to large until the condition

TABLE I
24 VVs SYNTHESIS PRINCIPLE

$\mathbf{V}_i$	Voltage vector				Ratios of each voltage vector			
$\mathbf{V}_i$	$\boldsymbol{u}_1$	$\boldsymbol{u}_2$	$\boldsymbol{u}_3$	$\boldsymbol{u}_0$	D_1	D_2	D_3	D_0
$\mathbf{V}_1$	$\boldsymbol{u}_{55}$	$\boldsymbol{u}_{45}$	$\boldsymbol{u}_{44}$	$\boldsymbol{u}_0$	0.034	0.443	0.477	0.046
$\mathbf{V}_2$	$\boldsymbol{u}_{44}$	$\boldsymbol{u}_{65}$	/	$\boldsymbol{u}_0$	0.723	0.264	0	0.013
$\mathbf{V}_3$	$\boldsymbol{u}_{44}$	$\boldsymbol{u}_{64}$	$\boldsymbol{u}_{66}$	$\boldsymbol{u}_0$	0.477	0.443	0.034	0.046
$\mathbf{V}_4$	$\boldsymbol{u}_{44}$	$\boldsymbol{u}_{64}$	$\boldsymbol{u}_{66}$	$\boldsymbol{u}_0$	0.264	0.458	0.264	0.014
$\mathbf{V}_5$	$\boldsymbol{u}_{44}$	$\boldsymbol{u}_{64}$	$\boldsymbol{u}_{66}$	$\boldsymbol{u}_0$	0.034	0.443	0.477	0.046
$\mathbf{V}_6$	$\boldsymbol{u}_{66}$	$\boldsymbol{u}_{24}$	/	$\boldsymbol{u}_0$	0.723	0.264	0	0.013
$\mathbf{V}_7$	$\boldsymbol{u}_{66}$	$\boldsymbol{u}_{26}$	$\boldsymbol{u}_{22}$	$\boldsymbol{u}_0$	0.477	0.443	0.034	0.046
$\mathbf{V}_8$	$\boldsymbol{u}_{66}$	$\boldsymbol{u}_{26}$	$\boldsymbol{u}_{22}$	$\boldsymbol{u}_0$	0.264	0.458	0.264	0.014
$\mathbf{V}_9$	$\boldsymbol{u}_{66}$	$\boldsymbol{u}_{26}$	$\boldsymbol{u}_{22}$	$\boldsymbol{u}_0$	0.034	0.443	0.477	0.046
$\mathbf{V}_{10}$	$\boldsymbol{u}_{22}$	$\boldsymbol{u}_{36}$	/	$\boldsymbol{u}_0$	0.723	0.264	0	0.013
$\mathbf{V}_{11}$	$\boldsymbol{u}_{22}$	$\boldsymbol{u}_{32}$	$\boldsymbol{u}_{33}$	$\boldsymbol{u}_0$	0.477	0.443	0.034	0.046
$\mathbf{V}_{12}$	$\boldsymbol{u}_{22}$	$\boldsymbol{u}_{32}$	$\boldsymbol{u}_{33}$	$\boldsymbol{u}_0$	0.264	0.458	0.264	0.014
$\mathbf{V}_{13}$	$\boldsymbol{u}_{22}$	$\boldsymbol{u}_{32}$	$\boldsymbol{u}_{33}$	$\boldsymbol{u}_0$	0.034	0.443	0.477	0.046
$\mathbf{V}_{14}$	$\boldsymbol{u}_{33}$	$\boldsymbol{u}_{12}$	/	$\boldsymbol{u}_0$	0.723	0.264	0	0.013
$\mathbf{V}_{15}$	$\boldsymbol{u}_{33}$	$\boldsymbol{u}_{13}$	$\boldsymbol{u}_{11}$	$\boldsymbol{u}_0$	0.477	0.443	0.034	0.046
$\mathbf{V}_{16}$	$\boldsymbol{u}_{33}$	$\boldsymbol{u}_{13}$	$\boldsymbol{u}_{11}$	$\boldsymbol{u}_0$	0.264	0.458	0.264	0.014
$\mathbf{V}_{17}$	$\boldsymbol{u}_{33}$	$\boldsymbol{u}_{13}$	$\boldsymbol{u}_{11}$	$\boldsymbol{u}_0$	0.034	0.443	0.477	0.046
$\mathbf{V}_{18}$	$\boldsymbol{u}_{11}$	$\boldsymbol{u}_{53}$	/	$\boldsymbol{u}_0$	0.723	0.264	0	0.013
$\mathbf{V}_{19}$	$\boldsymbol{u}_{11}$	$\boldsymbol{u}_{51}$	$\boldsymbol{u}_{55}$	$\boldsymbol{u}_0$	0.477	0.443	0.034	0.046
$\mathbf{V}_{20}$	$\boldsymbol{u}_{11}$	$\boldsymbol{u}_{51}$	$\boldsymbol{u}_{55}$	$\boldsymbol{u}_0$	0.264	0.458	0.264	0.014
$\mathbf{V}_{21}$	$\boldsymbol{u}_{11}$	$\boldsymbol{u}_{51}$	$\boldsymbol{u}_{55}$	$\boldsymbol{u}_0$	0.034	0.443	0.477	0.046
$\mathbf{V}_{22}$	$\boldsymbol{u}_{55}$	$\boldsymbol{u}_{41}$	/	$\boldsymbol{u}_0$	0.723	0.264	0	0.013
$\mathbf{V}_{23}$	$\boldsymbol{u}_{55}$	$\boldsymbol{u}_{45}$	$\boldsymbol{u}_{44}$	$\boldsymbol{u}_0$	0.477	0.443	0.034	0.046
$\mathbf{V}_{24}$	$\boldsymbol{u}_{55}$	$\boldsymbol{u}_{45}$	$\boldsymbol{u}_{44}$	$\boldsymbol{u}_0$	0.264	0.458	0.264	0.014

equation is not satisfied. For example, the magnitude can be set as $0.3U_{\rm dc}$, and all the ratios of the basic vector are greater than zero in each VV. However, the low-voltage utilization is obtained compared with the conventional 24-VV methods ($0.597U_{\rm dc}$). According to this principle, the magnitude of VV is gradually increased until the ratio is negative. After calculation, the final result of the magnitude is $0.59U_{\rm dc}$, which is close to the voltage utilization of the conventional method. In this case, 24 equal-magnitude VVs can be calculated offline, and the results are listed in Table I.

B. Duty Cycle Calculation With Minimum Error

Although the new 24 VVs increase the number of candidate voltage vectors, which extend the modulation range, however, the fixed magnitude limits the modulation range to 24 vertex positions. This shortcoming will deteriorate the steady-state performance. The issue can be solved by inserting $\mathbf{V}_0$ in one control period. The conventional deadbeat duty cycle calculation method diagram is shown in Fig. 7, where one active VV and one $\mathbf{V}_0$ are employed in one control period.

The red line represents the current increment using active VV, while the blue line indicates the current decrement by using $\mathbf{V}_0$. The q-axis current deadbeat principle is always adopted to be the constraint since only one unknown (d) is to be solved. However, the d-axis current is not taken into consideration, which is insufficient to improve operational performance.

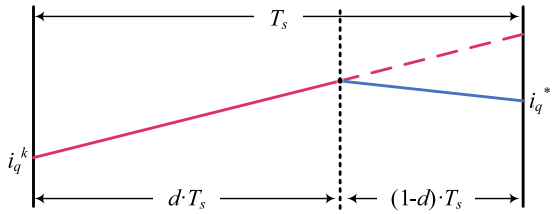

Fig. 7. Diagram of the conventional deadbeat duty cycle calculation method.

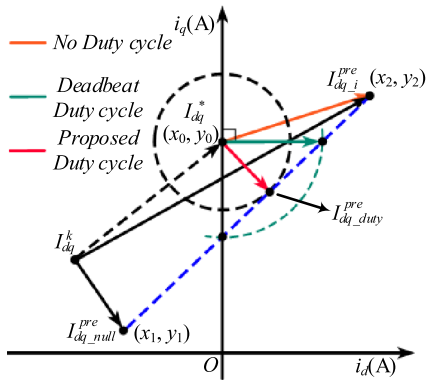

Fig. 8. Cost function value of different duty cycle calculation methods.

To further enhance the control system, a minimum error duty cycle calculation method is proposed in this section. As shown in Fig. 8, the I_{dq}^k and I_{dq}^* are marked in the dq coordinate system. The $I_{dq\_i}^{\rm pre}$ and $I_{dq\_\rm null}^{\rm pre}$ are the predictive values of I_{dq} under the action of the $\mathbf{V}_i$ and $\mathbf{V}_0$, respectively. It should be noted that the trajectory of the modulated voltage vector is located on the blue dotted line. The distance from the point on the trajectory to point I_{dq}^* can be expressed as

$$l = \sqrt{\left(i_d^* - i_d^{\rm pre}\right)^2 + \left(i_q^* - i_q^{\rm pre}\right)^2}. \tag{12}$$

On the other aspect, for the PMSM, whether implanted or surface mounted, the cost function of VV-based MPC can be expressed as

$$J = \left(i_d^* - i_d^{\rm pre}\right)^2 + \left(i_q^* - i_q^{\rm pre}\right)^2. \tag{13}$$

It can be deduced from (12) and (13) that the l^2 equals the cost function in the MPC scheme, and $J \in [l_{\min}^2, l_{\max}^2]$. That means, l is positively correlated with J. Hence, there is an optimal point on the trajectory that minimizes the value of the cost function. Draw a circle with center I_{dq}^* and radius l. All the points in this circle have the same value of J. Obviously, the tangent point is the closest to the reference value. If the final predicted value is located at this point, its cost function will be the minimum of all points on the trajectory. So, in order to obtain the optimal value of the cost function, the tangent point needs to be calculated.

For simplicity, the coordinates of the I_{dq}^*, $I_{dq\_\rm null}^{\rm pre}$, and $I_{dq\_i}^{\rm pre}$ are represented by (x_0, y_0), (x_1, y_1), and (x_2, y_2), respectively. Therefore, the position of the tangent point can be calculated by

TABLE II
SPECIFIC VOLTAGE VECTORS IN DIFFERENT GROUPS

Group	Voltage vectors
G_1	$\mathbf{V}_{22}$, $\mathbf{V}_{23}$, $\mathbf{V}_{24}$, $\mathbf{V}_1$, $\mathbf{V}_2$, $\mathbf{V}_3$, $\mathbf{V}_4$
G_2	$\mathbf{V}_4$, $\mathbf{V}_5$, $\mathbf{V}_6$, $\mathbf{V}_7$, $\mathbf{V}_8$, $\mathbf{V}_9$, $\mathbf{V}_{10}$
G_3	$\mathbf{V}_{10}$, $\mathbf{V}_{11}$, $\mathbf{V}_{12}$, $\mathbf{V}_{13}$, $\mathbf{V}_{14}$, $\mathbf{V}_{15}$, $\mathbf{V}_{16}$
G_4	$\mathbf{V}_{16}$, $\mathbf{V}_{17}$, $\mathbf{V}_{18}$, $\mathbf{V}_{19}$, $\mathbf{V}_{20}$, $\mathbf{V}_{21}$, $\mathbf{V}_{22}$

the geometric relationship and described as

$$\begin{cases} i_{d\_\text{duty}}^{\text{pre}} = \dfrac{x_0(x_1-x_2)^2+x_1(y_1-y_2)^2+(x_1-x_2)(y_1-y_0)(y_2-y_1)}{(x_1-x_2)^2+(y_1-y_2)^2} \\ i_{q\_\text{duty}}^{\text{pre}} = \dfrac{y_0(y_1-y_2)^2+y_1(x_1-x_2)^2+(x_1-x_0)(x_1-x_2)(y_2-y_1)}{(x_1-x_2)^2+(y_1-y_2)^2} \end{cases} \tag{14}$$

with

$$x_0 = i_d^*, y_0 = i_q^*$$

$$x_1 = i_d^{k+1} + T_s \cdot \left[-R_s i_d^{k+1} + \omega_e L_q i_q^{k+1}\right] / L_d$$

$$y_1 = i_q^{k+1} + T_s \cdot \left[-R_s i_q^{k+1} - \omega_e L_d i_d^{k+1} - \omega_e \psi_f\right] / L_q$$

$$x_2 = i_d^{k+1} + T_s \cdot \left[u_d^{k+1} - R_s i_d^{k+1} + \omega_e L_q i_q^{k+1}\right] / L_d$$

$$y_2 = i_q^{k+1} + T_s \cdot \left[u_q^{k+1} - R_s i_q^{k+1} - \omega_e L_d i_d^{k+1} - \omega_e \psi_f\right] / L_q.$$

The duty cycle of $\mathbf{V}_0$ and $\mathbf{V}_i$ can be obtained as

$$d_1 = \left|(x_1 - i_d^{\text{duty}})/(x_1 - x_2)\right|, d_0 = 1 - d_1. \tag{15}$$

The cost function value of different duty cycle calculation methods is marked in Fig. 8 with three color lines (orange, green, and red). The orange line represents no duty cycle method, and its current tracking error is the largest. The green line is perpendicular to the q-axis, which takes the deadbeat tracking of the q-axis current as the modulation target and does not consider the constraint of the d-axis current. Also, there are two intersections for the circle and line, which result in two different duty cycles that can obtain the same J. So, the current tracking error is second. The red line is the proposed method, which takes the minimum dq-axis current error as the modulation target. Hence, the proposed method has the smallest current tracking error and can better improve operational performance.

C. Simplified Evaluation Process

In the MPC scheme, the cost function is the evaluation standard of the voltage vector. The different voltage vectors will cause different changes for control variables in the future instant, such as i_q and i_d. The voltage vector, whose changes are closest to the reference value, is the optimal one. In the evaluation process, the value of the cost function is obtained using the for-cycle structure. So, without any simplification, it would take 24 cycles to complete this repetitive work since 24 VVs are in the control set. In order to solve this problem, a multistage group evaluation method is proposed to release the time-consuming work. The detailed implementation of the simplified process can be divided into the following steps.

First, the 24 VVs are divided into four groups evenly. The voltage vectors for each group are listed in Table II, and the diagram is shown in Fig. 9(a). The cost function evaluates the central voltage vector of each group to select the optimal group. The evaluation process will take four cycles, and the flowchart is shown in Fig. 10.

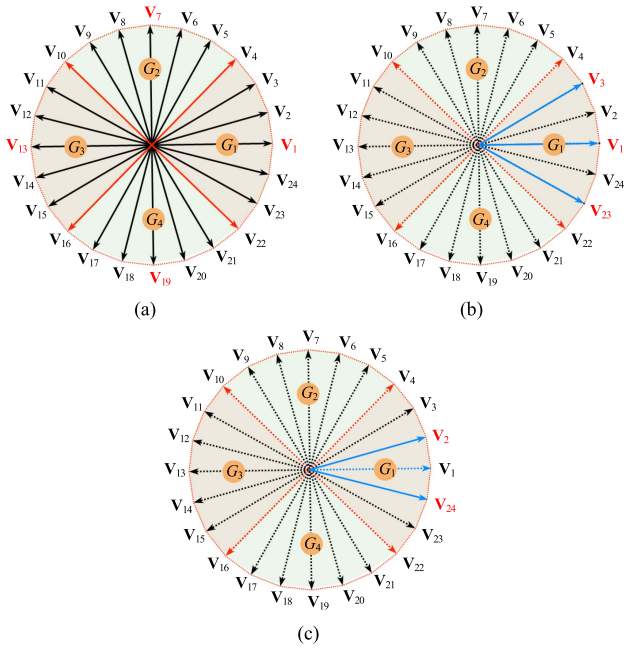

Fig. 9. Diagram of simplified method. (a) Group division. (b) Optimal group. (c) $\mathbf{V}_{2\text{nd}}$ selection.

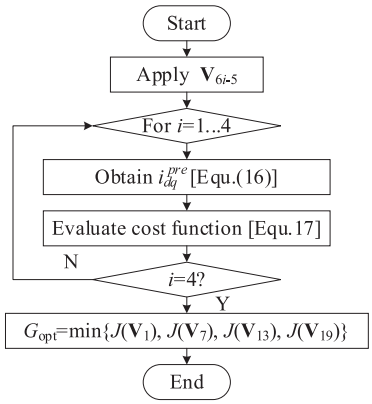

Fig. 10. Flowchart of the process for optimal group selection.

Second, the voltage vector in the optimal group is divided into the odd-numbered and even-numbered groups again. Take the $G_{\text{opt}} = G_1$, for example, as shown in Fig. 9(b). The odd-numbered group contains $\mathbf{V}_{22}$, $\mathbf{V}_{24}$, and $\mathbf{V}_2$, while $\mathbf{V}_{23}$, $\mathbf{V}_1$, and $\mathbf{V}_3$ are included in the even-numbered group. Then, the cost function is used again to evaluate $\mathbf{V}_3$ and $\mathbf{V}_{23}$ (the cost function result of $\mathbf{V}_1$ does not need to be recalculated since the result has been obtained in the process of G_{opt} selection) to select the optimal one, named $V_{1\text{st}}$. The flowchart of G_1 is shown in Fig. 11, and the other case has the same structure as the flowchart of G_1.

Finally, the cost function is used again to evaluate the two voltage vectors adjacent to $\mathbf{V}_{1\text{st}}$, named $\mathbf{V}_{2\text{nd}}$, and compare them

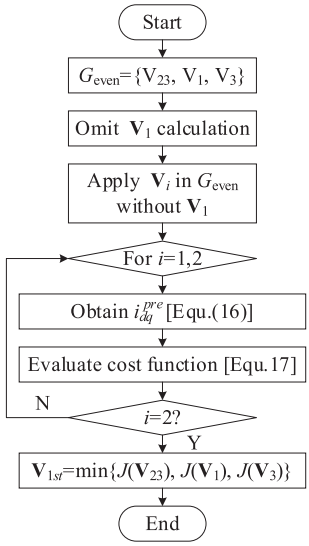

Fig. 11. Flowchart of the process for $\mathbf{V}_{1st}$ selection.

TABLE III
ALL SITUATIONS OF SELECTING OPTIMAL VECTOR

Group	$\mathbf{V}_{1st}$	$\mathbf{V}_{2nd}$
	$\mathbf{V}_1$	$\mathbf{V}_2$ or $\mathbf{V}_{24}$
$G_1(\mathbf{V}_1)$	$\mathbf{V}_3$	$\mathbf{V}_2$ or $\mathbf{V}_4$
	$\mathbf{V}_{23}$	$\mathbf{V}_{22}$ or $\mathbf{V}_{24}$
	$\mathbf{V}_5$	$\mathbf{V}_4$ or $\mathbf{V}_6$
$G_2(\mathbf{V}_7)$	$\mathbf{V}_7$	$\mathbf{V}_6$ or $\mathbf{V}_8$
	$\mathbf{V}_9$	$\mathbf{V}_8$ or $\mathbf{V}_{10}$
	$\mathbf{V}_{11}$	$\mathbf{V}_{10}$ or $\mathbf{V}_{12}$
$G_3(\mathbf{V}_{13})$	$\mathbf{V}_{13}$	$\mathbf{V}_{12}$ or $\mathbf{V}_{14}$
	$\mathbf{V}_{15}$	$\mathbf{V}_{14}$ or $\mathbf{V}_{16}$
	$\mathbf{V}_{17}$	$\mathbf{V}_{16}$ or $\mathbf{V}_{18}$
$G_4(\mathbf{V}_{19})$	$\mathbf{V}_{19}$	$\mathbf{V}_{18}$ or $\mathbf{V}_{20}$
	$\mathbf{V}_{21}$	$\mathbf{V}_{20}$ or $\mathbf{V}_{22}$

with $\mathbf{V}_{1st}$ to select the final optimal voltage vector. Fig. 9(c) shows the example of $\mathbf{V}_{1st} = \mathbf{V}_1$, where $\mathbf{V}_2$ and $\mathbf{V}_{24}$ are evaluated using the cost function. The final optimal vector is the result of $\mathbf{V}_{opt} = \min\{J(\mathbf{V}_1), J(\mathbf{V}_2), J(\mathbf{V}_{24})\}$.

All the situations for selecting the optimal vector are listed in Table III. The tedious enumeration of the conventional MPC can be avoided by using the proposed vector selection method. The number of the evaluation process can be reduced from 24 to $8(4 + 2 + 2)$. The proposed simplified evaluation process can significantly reduce the number of cycles and the execution time of the algorithm.

D. Implementation of the Proposed Method

Since the duty cycle method is designed, the magnitude of candidate vectors can be flexible and changed. In order to finely select the most suitable vector and its corresponding duty cycle, the control sets are modified as $d_1\mathbf{V}_1$, $d_2\mathbf{V}_2$, $d_3\mathbf{V}_3$, …,$d_{24}\mathbf{V}_{24}$. When the VV method is employed, the components on the xy-subspace can be omitted in the predictive model. Hence, the predictive model of DTP-PMSM with two-step prediction can

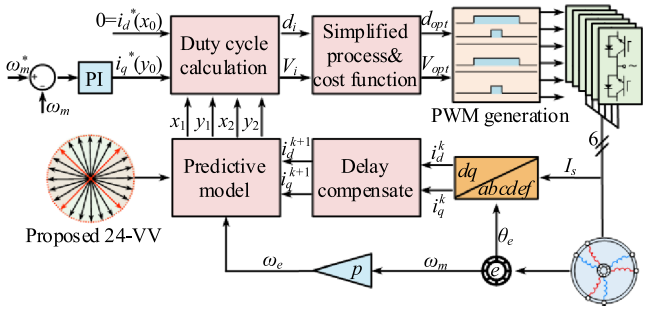

Fig. 12. Control block diagram of the proposed MPC.

TABLE IV
PARAMETERS OF EXPERIMENTAL MOTOR AND DRIVES SYSTEM

Parameters	Value	Parameters	Value
d-axes inductances	15.2 mH	Number of pole pairs	11
q-axes inductances	15.7 mH	DC bus	300 V
Rotor flux	0.88 Wb	Period of PWM	100 us
Stator resistance	0.96 Ω	Sample frequency	10 kHz

be expressed as

$$\begin{cases} i_d^{k+2} = i_d^{k+1} + T_s\left[d_i u_{di}^{k+1} - R_s i_d^{k+1} + \omega_e L_q i_q^{k+1}\right]/L_d \\ i_q^{k+2} = i_q^{k+1} \\ \quad + T_s\left[d_i u_{qi}^{k+1} - R_s i_q^{k+1} - \omega_e L_d i_d^{k+1} - \omega_e \psi_f\right]/L_q. \end{cases} \tag{16}$$

In order to calculate the distance from the reference point to the tangent point more clearly, the cost function of the proposed MPC scheme can be expressed as

$$g' = l = \sqrt{\left(i_d^* - i_d^{k+2}\right)^2 + \left(i_q^* - i_q^{k+2}\right)^2}. \tag{17}$$

The proposed modified MPC scheme can obtain the optimal cost function by calculating the duty cycles. It reduces predictive errors and improves control precision. The control block diagram of the proposed MPC scheme is shown in Fig. 12. The implementation process can be summarized as follows.

1) Delay compensation: The i_d^k and i_q^k are compensated by the delay compensate module to obtain i_d^{k+1} and i_q^{k+1}.
2) Predictive model: The values of x_1, y_1, x_2, and y_2 are calculated by the predictive model.
3) Duty cycle calculation: The duty cycle of evaluated VV can be calculated after the (x_0, y_0), (x_1, y_1), and (x_2, y_2) are determined.
4) Evaluation process: The cost function is used to evaluate the modified VV and also simplify this evaluation process to release the computational burden.

IV. EXPERIMENTAL VERIFICATION

An experimental platform is established to verify the proposed method, as shown in Fig. 13. A DTP-PMSM is fed by a six-phase voltage-source inverter. The magnetic power brake is used as the load. The parameters of the experimental motor and drive system are listed in Table IV. All algorithms are implemented on the TMS320F28377 DSP. The phase current is measured using

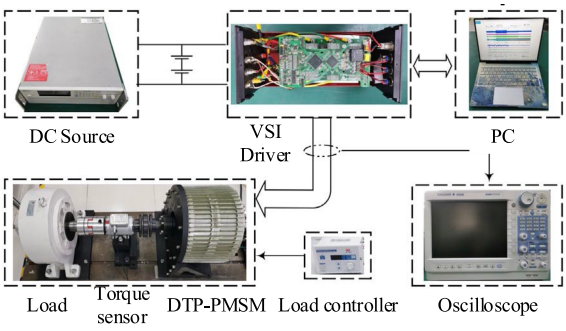

Fig. 13. Schematic diagram of the experimental platform.

a current probe. The i_d, i_q, i_x, i_y, and torque are obtained by the D/A converter. The calculation formula of torque can be expressed as

$$T_e = 3n_p\left[(L_d - L_q)i_d i_q + \psi_f i_q\right]. \tag{18}$$

For detailed quantitative analysis, the total harmonic distortion (THD) analysis is calculated, where the original data are recorded from the experiment. Also, the *dq*-axis currents, *xy*-axis currents, torque, and current ripple are calculated by standard deviation, respectively. The equation is shown as

$$X_{\text{ripple}} = \sqrt{\frac{1}{n}\sum_{i=1}^{n}\left(X_i - \bar{X}\right)^2} \tag{19}$$

where X represents the *dq* axes' currents, *xy* axes' currents, and electromagnetic torque, respectively.

A. Steady-State Performance

In the steady-state performance experiment, the speed is 100 r/min, and the load is 200 N·m. For fairness, the proportional integral (PI) controller parameters used in MPC are the same and equal to those of the FOC speed-loop PI controller. The K_p is 0.12, and K_i is 0.003. The waveforms of *dq* axes' currents, *xy* axes' currents, torque, and phase-*A* currents are recorded. The THD of phase-*A* current is analyzed, and the flux trajectory in the stationary and rotating coordinate system is also plotted. The action of the upper switch of the phase-*A* bridge leg is also recorded.

The classical 24 VVs are first conducted, and the duty cycle calculation method of Fig. 7 is selected. The experimental results are shown in Fig. 14. As can be seen from this figure, the phase current presents obvious harmonic components. The result of THD is 10.8% by Fourier analysis, where the fifth harmonics is 4.3%, and the seventh harmonics is 8.4%. The peak value of harmonic current reaches ±1.5 A and the ripple of i_x and i_y calculated by (18) are 0.54 A and 0.55 A, respectively. Correspondingly, the area of flux in the harmonic subspace is relatively large. This is because the distribution of vectors in the classical 24 VVs is shown in Fig. 2. When the duty cycle modulation technique is introduced, the inner VV can be regarded as the equivalent voltage vector by the outer VV. In this case, the classical 24 VVs causes a waste of voltage vectors. Finally, it

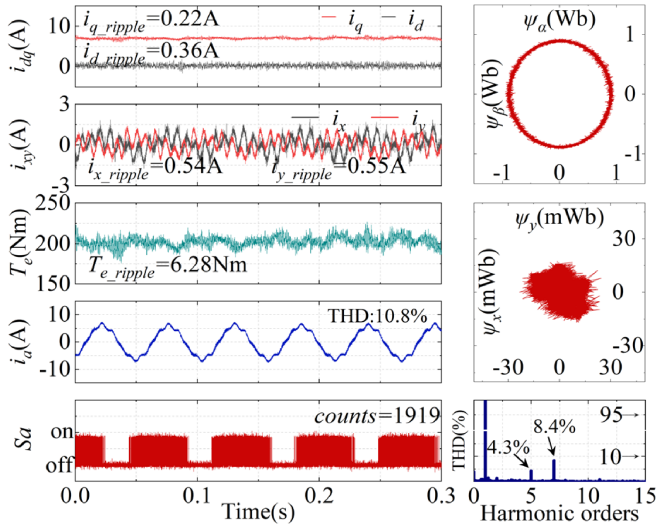

Fig. 14. Steady-state performance of classical 24-VV method when deadbeat duty cycle method is applied.

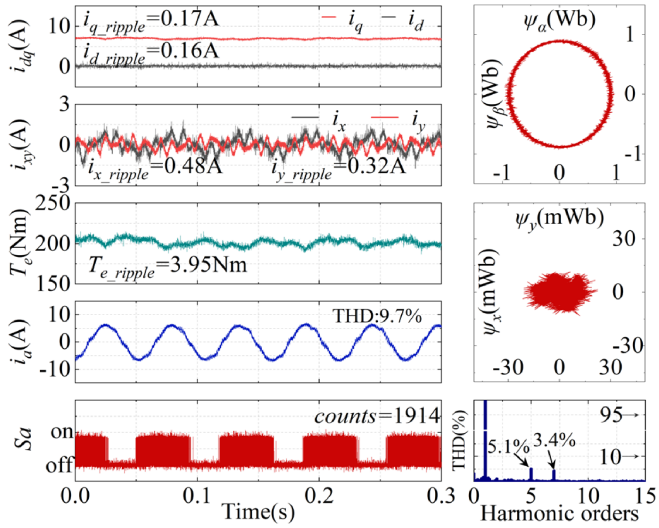

Fig. 15. Steady-state performance of the proposed 24-VV method when the deadbeat duty cycle method is applied.

is equivalent to only the outermost 12 VVs at work. Currently, the torque ripple is 6.28 N·m, and the ripples of i_d and i_q are 0.36 A and 0.22 A, respectively. The states of flux and switches are also plotted in Fig. 14. In this section, all the performance indicators of Fig. 14 are selected as a reference to evaluate the effectiveness of the proposed methods.

In order to verify the proposed 24-VV method, the second experiment maintains the conventional duty cycle calculation method. The control sets are replaced by the distribution in Fig. 6. The experimental results are depicted in Fig. 15. Compared with Fig. 14, the ripples of the phase current are reduced, and the waveform becomes more sinusoidal. After quantitative analysis, the fifth harmonics rise slightly, while the seventh harmonics are reduced significantly. The final THD is reduced to 9.7%. In addition, the ripples of i_x and i_y are also reduced

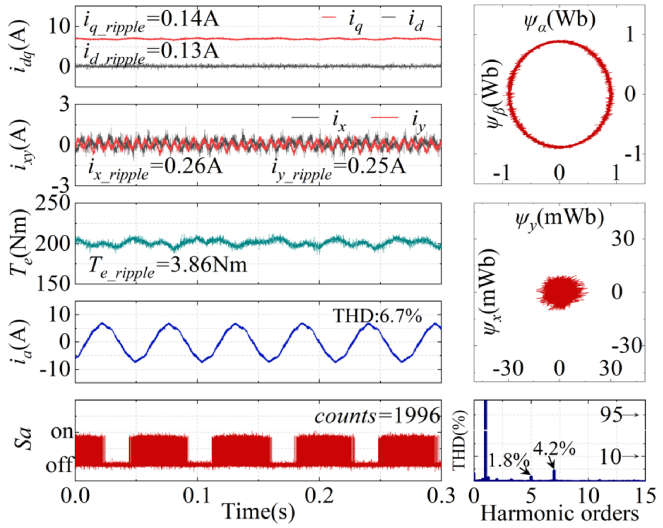

Fig. 16. Steady-state performance of the proposed 24-VV method when minimum error duty cycle method is applied.

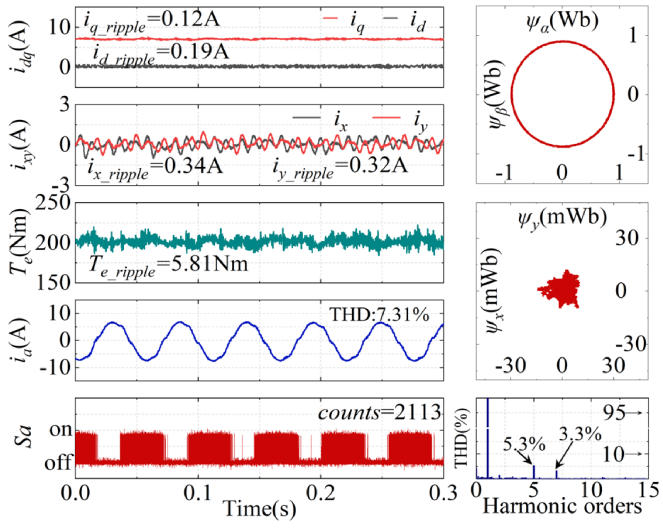

Fig. 17. Steady-state performance of multivector-based MPC.

to 0.48 A and 0.32 A, respectively. However, the performance improvement of the fundamental subspace is more significant. The ripples of i_d and i_q are 0.16 A and 0.17 A, respectively. The torque ripple is reduced from 6.28 to 3.95 N·m, which is improved by 37% points. The improvement is because the proposed 24-VV scheme has a dense vector distribution. Compared with the conventional 24-VV distribution, the torque increment is more stable in the process of vector switching. Also, the proposed distribution still fully utilizes all the voltage vectors under the duty cycle modulation. The broader modulation area can be covered, effectively enhancing operational performance. Also, it can be seen from the state of the switches in the phase-*A* bridge leg that the switching loss does not increase. This experiment can prove the effectiveness of the proposed 24-VV distribution.

The following experiment is prepared to verify the validity of the proposed duty cycle calculation method. In this experiment, the vector distribution in Fig. 6 is adopted, while the duty cycle is calculated by the geometric method, as shown in Fig. 8. Therefore, the comparative experiment of this part is Fig. 15. The results are shown in Fig. 16. Since only the duty cycle calculation method is changed, the switching loss is almost unchanged. However, as can be seen from Fig. 16, the phase current has a narrower envelope. The THD is reduced to 6.7%, which indicates that the components of harmonic current are improved. The decrease in the ripples of i_x and i_y also confirms this. Moreover, torque ripple and *dq*-axis currents have been slightly enhanced as well. Compared with the above two experiments, the area of flux in the harmonic subspace is reduced, and the flux circle is improved. Results show that the minimum error duty cycle method has better control performance. This is because the i_d is considered in the duty cycle calculation process. The duty cycle calculation of the vector is more accurate through the cost function selection. The result of this duty cycle presents a minimum error. Consequently, the performance can be further

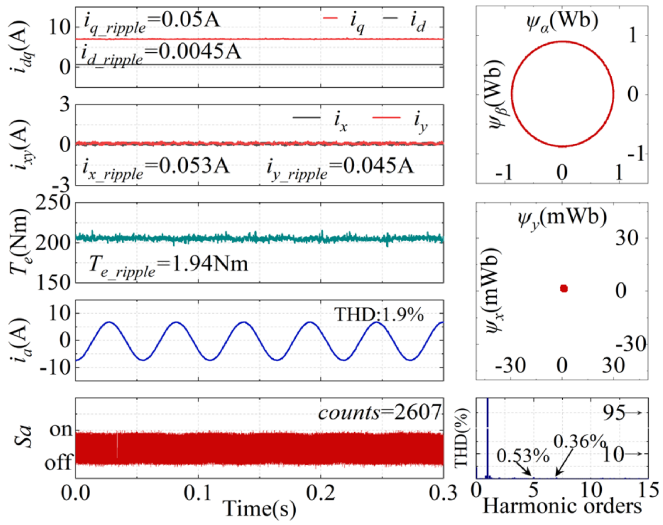

Fig. 18. Steady-state performance of FOC.

improved. The results show the effectiveness of the proposed minimum error duty cycle method.

To further verify the effectiveness of the proposed method, the multivector-based MPC introduced in [32] is also tested. In this experiment, two active VVs and a null vector are used in one control period. Therefore, the switching frequency is the same as the previous algorithms for fairness. The results are shown in Fig. 17. Compared with the proposed 24-VV scheme, the ripple of i_q is reduced, while the id ripple increases. The total reluctance torque ripple will increase due to the different *dq*-axis inductances, increasing the final torque ripple. This is because the control frequency needs to be reduced appropriately to maintain the same switching frequency. Moreover, the control set of the multivector-based MPC only contains 12 VVs. The torque increment still exists in the process of vector switching.

Fig. 18 shows the results of the FOC algorithm. The best steady-state performance can be achieved. The phase current

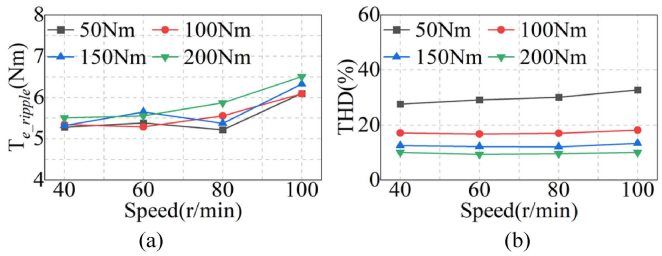

Fig. 19. Steady-state performance of the conventional 24 VVs under different conditions. (a) Results of torque ripple. (b) Results of THD.

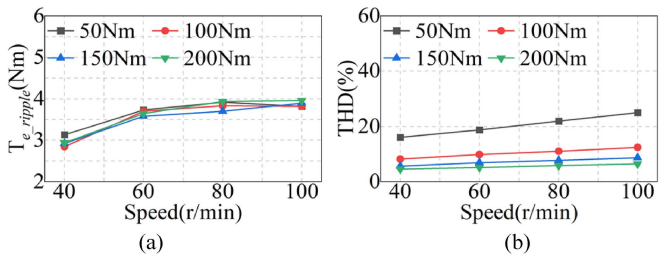

Fig. 20. Steady-state performance of the proposed method under different conditions. (a) Results of torque ripple. (b) Results of THD.

presents a perfect sinusoidal waveform, and the flux trajectory is close to the standard circle. Other performance indicators are all better than the MPC algorithm. This is because the FOC is a harmonic subspace closed-loop scheme. The harmonic subspace is essentially an open-loop control structure in MPC since the introduction of VV technology. Moreover, the FOC is a continuous method, superior to the finite-control-set MPC in steady-state performance. However, the FOC method is more complex in parameter adjustment. For the dual three-phase motor system, five parameters of PI controllers need to be adjusted. On the one hand, the speed regulation range is limited by the bandwidth of the controller. On the other hand, the parameter adjustment process costs massive effort. It can be seen from the test results of FOC, that the switching loss of FOC is greater than that of the MPC. In some high-demand conditions, the FOC may not be qualified.

In addition, the classical 24-VV and proposed methods are tested under multiple conditions to prove the universality of the proposed strategy. In this experiment, the speed is set at 40 r/min, 60 r/min, 80 r/min, and 100 r/min, respectively, while the load is set at 50 N·m, 100 N·m, 150 N·m, and 200 N·m, respectively. The results of torque ripple and THD are exhibited in Figs. 19 and 20. As can be seen from Figs. 19(a) and 20(a), there is an overall upward trend in torque ripple as the speed increases. In Figs. 19(a) and 20(a), the THD is increased with load decreased regardless of any speed. However, the proposed method presents a lower torque ripple than the classical 24-VV method in any case. Moreover, there is only a slight change in THD for the same load at different speeds in Figs. 19(b) and 20(b). In general, although the steady-state performance of the motor is reduced at low loads and speeds, the proposed method has an obvious advantage over the classical one.

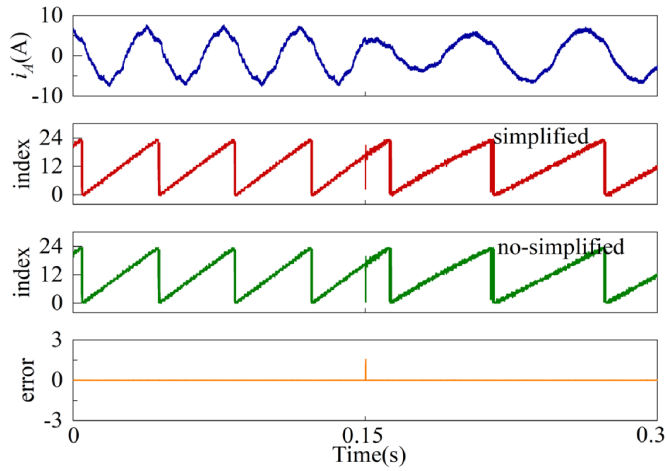

Fig. 21. Results of optimal VV selection.

B. Execution Time Test

To verify the feasibility of the proposed simplified evaluation method, the optimal voltage vector selected with and without the simplified method is tested. The speed is changed from 150 to 100 r/min, and the load is still 200 N·m. In the no-simplified method, 24 VVs are evaluated individually until the optimal vector is selected. The simplified method is the proposed multistage evaluation process. Fig. 21 presents the optimal voltage vector selection process, where the orange waveform represents the errors of different methods. It can be seen from the results that the error only exists during transient speed switching. When the motor is operated at a steady state, the different evaluated methods select the same voltage vector. Hence, the results prove that the proposed simplified evaluation method will not lose optimality.

The execution time of 12-VV MPC, classical 24-VV, and proposed simplified 24-VV MPC is also tested. In this experiment, a pin reversal signal is set before and after the algorithm in the DSP programming to measure the execution time. The tested process of the algorithm includes "two-step prediction," "duty cycle calculation," and "evaluation process." When the algorithm program is entered, timing starts, and the pin outputs a high level. The timing ends at the above-mentioned process end, and the pin outputs a low level. The duration of the high level measured by the oscilloscope is plotted in Fig. 22. The executing time of the FOC is 6.5 μs. Compared with the other MPC methods, the FOC strategy has the least execution time since there is no evaluation process for all voltage vectors. In the MPC scheme, the for-cycle structure was employed during the process of evaluating voltage vectors. When 24 candidate VVs are employed in the classical MPC and without using the simplified method, the for-cycle needs to be executed 24 times. This is a redundant process, and the tested executing time is 41 μs. However, when the proposed simplified method is introduced, the executing time of the proposed simplified 24-VV MPC reduces to 14.7 μs. Also, the execution time of the 12-VV MPC method is measured. Results show that the multistage group evaluation method has advantages over the conventional

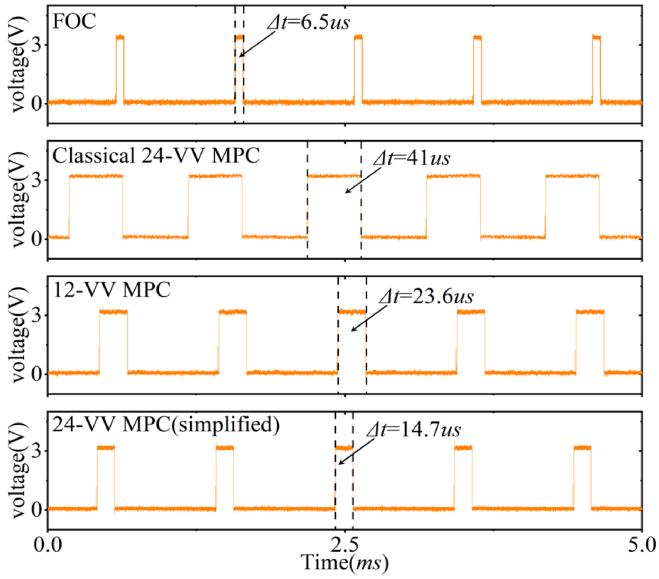

Fig. 22. Execution time of different methods.

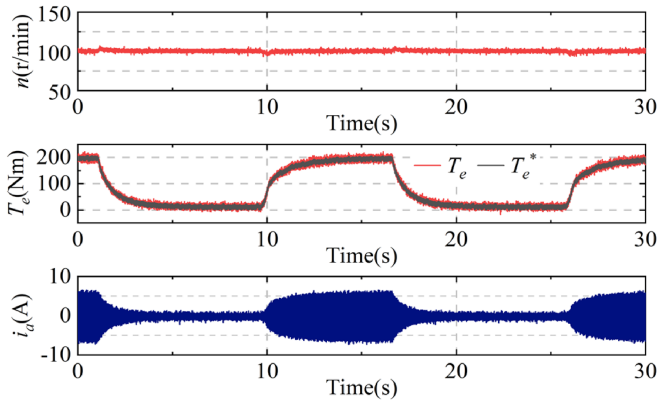

Fig. 23. Load-step experiment of the classical 24-VV method when deadbeat duty cycle method is applied.

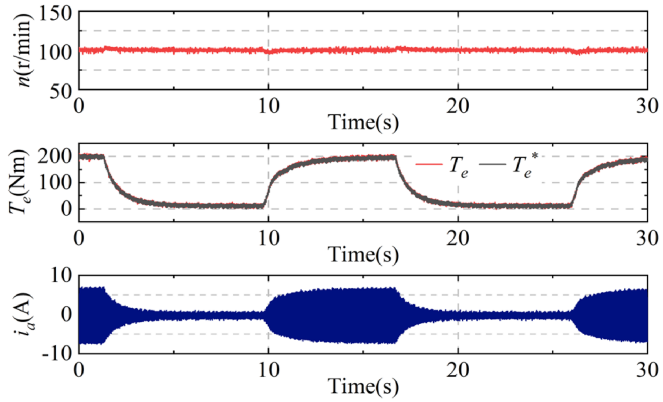

Fig. 24. Load-step experiment of the proposed 24-VV method when minimum error duty cycle method is applied.

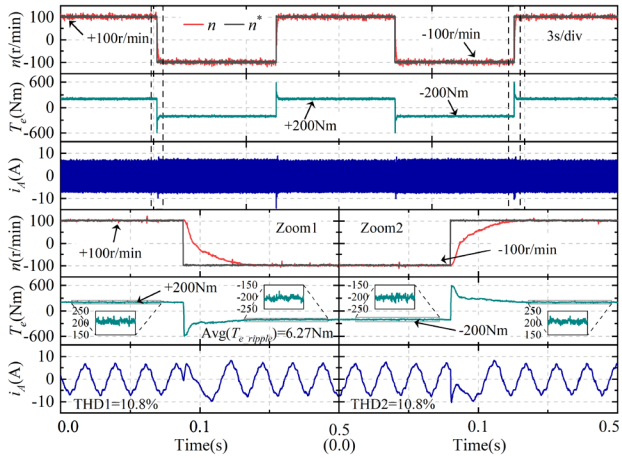

Fig. 25. Speed reversal experiment of the classical 24-VV method when deadbeat duty cycle method is applied.

12-VV MPC in the execution time. That is because only eight vectors are involved in the evaluation process.

C. Dynamic Performance

In this section, the transient experiments of the classical 24-VV method with deadbeat duty cycle calculation and the proposed method are conducted to validate the dynamic performance.

The load-step experiment is conducted. The speed is still 100 r/min. The load is 200 N·m first, and then switch OFF the controller of the magnetic powder brake to simulate load changes. The dynamic response waveforms are illustrated in Figs. 23 and 24. The torque command is well tracked in both the conventional and proposed methods. Besides, the speed can reach its given command in a short time. However, the proposed method has a narrower torque curve envelope, suggesting a better steady-state performance than the conventional method.

The dynamic response experiment with speed step is tested first. The load torque is 200 N·m, and the speed changes from +100 to −100 r/min. The transient-state waveforms of the speed, torque, and phase current are recorded in Figs. 25 and 26. In order to facilitate the comparison, the torque waveform is locally amplified, and the average value of the four-segment torque ripple is calculated. The THD is also analyzed. The transient duration of these two methods is almost the same. In different speed conditions, the torque ripple and THD of the proposed method are much smaller than that of the conventional method, which means that the proposed method has better steady-state performance during the whole process.

Moreover, the experiment of speed and load changing at the same time is designed. In this experiment, the load torque changes from 200 to 0 N·m, and the speed changes from +100 to +50 r/min. The proposed 24-VV method is used when the minimum error duty cycle method is applied. The experimental results are recorded in Fig. 27. It can be seen from Fig. 27 that, although the speed and load change at the same time, the proposed algorithm still follows the reference command in

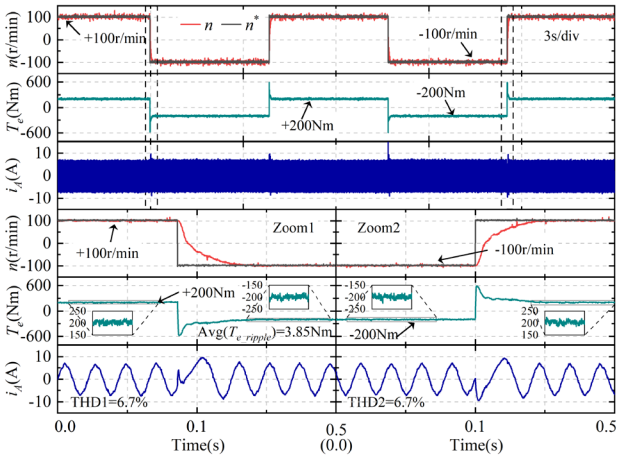

Fig. 26. Speed reversal experiment of the proposed 24-VV method when minimum error duty cycle method is applied.

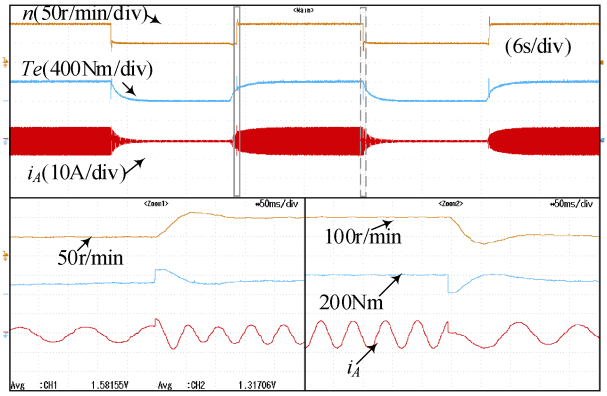

Fig. 27. Speed and load changing at the same time of the proposed 24-VV method when minimum error duty cycle method is applied.

a short time. It shows that the proposed algorithm has good reliability.

According to the transient experiments, a fast-dynamic response of the proposed method can be guaranteed. The proposed method provides much better steady-state performance without losing any dynamic characteristics and reliability.

D. Parameter Variation Analysis

The MPC method relies on precise machine parameters to select appropriate VVs. However, it is difficult to implement the accurate parameters in practice due to the variations injected by noise or temperature. Hence, it is necessary to evaluate the parameter sensitivity of the proposed method.

In this section, the parameter variation experiments are conducted. The inductance, stator resistor, and rotor flux increased by 120% magnitude and reduced to 80% after a few seconds. The waveform of speed, torque, and phase current is recorded. The results are exhibited in Fig. 28. The results show that the operation performance of the proposed algorithm is not obviously affected when the parameter mismatch reaches 20%.

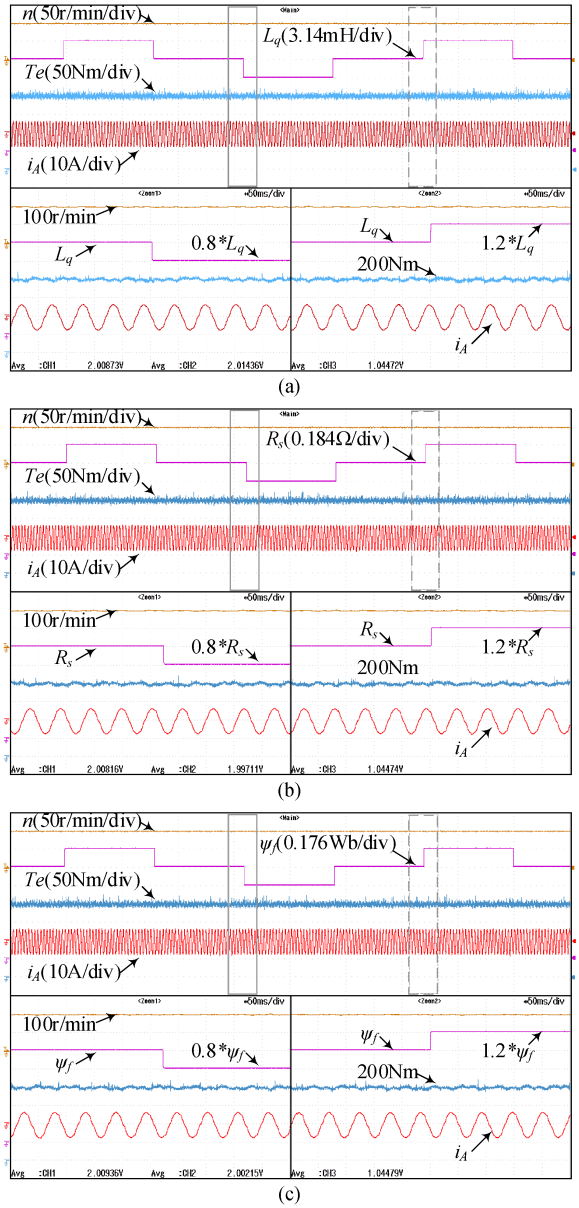

Fig. 28. Performance of the parameter variations for the proposed method. (a) Inductance. (b) Stator resistance. (c) Rotor flux.

This indicates that the proposed 24-VV scheme and duty cycle calculation method have good robustness.

V. Conclusion

In this article, an optimized 24-VV MPC with a minimum error duty cycle strategy has been proposed and implemented. This work can be concluded as follows.

1) The conventional VV distribution is replaced by the designed distribution. The new 24 VVs have the same magnitude, and the angle between each two adjacent vectors reduces to 15°. In this distribution mode, the torque ripple is improved.
2) A minimum error duty cycle method is proposed. The i_d can still be considered in duty cycle calculation, although

the single VV is adopted. The results of the duty cycle can be calculated more accurately.

3) A simplified vector evaluation method for MPC is proposed. The experimental results show that the simplified method costs a shorter execution time and has good feasibility.
4) Comprehensive experiments are carried out to verify the effectiveness of the proposed method.

REFERENCES

[1] Z. Song, Y. Jia, and C. Liu, "Open-phase fault-tolerant control strategy for dual three-phase permanent magnet synchronous machines without controller reconfiguration and fault detection," *IEEE Trans. Power Electron.*, vol. 38, no. 1, pp. 789–802, Jan. 2023.

[2] J. Cui, J. Ji, W. Zhao, T. Tao, L. Huang, and H. Tang, "Decoupled fault-tolerant model predictive current control for dual three-phase PMSMs with harmonic compensation," *IEEE Trans. Power Electron.*, vol. 38, no. 2, pp. 2285–2294, Feb. 2023.

[3] W. Li, G. Feng, Z. Li, J. Tjong, and N. C. Kar, "Multireference frame based open-phase fault modeling and control for asymmetrical six-phase interior permanent magnet motors," *IEEE Trans. Power Electron.*, vol. 36, no. 10, pp. 11712–11725, Oct. 2021.

[4] S. Saeed, W. Zhao, H. Wang, T. Tao, and F. Khan, "Fault-tolerant deadbeat model predictive current control for a five-phase PMSM with improved SVPWM," *Chin. J. Elect. Eng.*, vol. 7, no. 3, pp. 111–123, Sep. 2021.

[5] M. Hu, W. Hua, G. Ma, S. Xu, and W. Zeng, "Improved current dynamics of proportional-integral-resonant controller for a dual three-phase FSPM machine," *IEEE Trans. Ind. Electron.*, vol. 68, no. 12, pp. 11719–11730, Dec. 2021.

[6] Z. Liu, S. Shi, S. Yan, W. Sun, D. Jiang, and R. Qu, "A novel four-leg inverter topology for dual three-phase PMSM," *IEEE Trans. Power Electron.*, vol. 38, no. 2, pp. 2295–2306, Feb. 2023.

[7] Y. Zhao and T. Lipo, "Space vector PWM control of dual three-phase induction machine using vector space decomposition," *IEEE Trans. Ind. Appl.*, vol. 31, no. 5, pp. 1100–1109, Sep./Oct. 1995.

[8] S. Liu and C. Liu, "Virtual-vector-based robust predictive current control for dual three-phase PMSM," *IEEE Trans. Ind. Electron.*, vol. 68, no. 3, pp. 2048–2058, Mar. 2021.

[9] A. Habib et al., "Predictive current control of six-phase IM-based non-isolated integrated on-board battery charger under different winding configurations," *IEEE Trans. Power Electron.*, vol. 37, no. 7, pp. 8345–8358, Jul. 2022.

[10] Z. Sun, Y. Deng, J. Wang, T. Yang, Z. Wei, and H. Cao, "Finite control set model-free predictive current control of PMSM with two voltage vectors based on ultralocal model," *IEEE Trans. Power Electron.*, vol. 38, no. 1, pp. 776–788, Jan. 2023.

[11] F. Barrero, M. R. Arahal, R. Gregor, S. Toral, and M. J. Duran, "A proof of concept study of predictive current control for VSI-driven asymmetrical dual three-phase AC machines," *IEEE Trans. Ind. Electron.*, vol. 56, no. 6, pp. 1937–1954, Jun. 2009.

[12] Y. Ren and Z. Q. Zhu, "Enhancement of steady-state performance in direct-torque-controlled dual three-phase permanent-magnet synchronous machine drives with modified switching table," *IEEE Trans. Ind. Electron.*, vol. 62, no. 6, pp. 3338–3350, Jun. 2015.

[13] I. Gonzalez-Prieto, M. J. Duran, J. J. Aciego, C. Martin, and F. Barrero, "Model predictive control of six-phase induction motor drives using virtual voltage vectors," *IEEE Trans. Ind. Electron.*, vol. 65, no. 1, pp. 27–37, Jan. 2018.

[14] P. F. C. Gonçalves, S. M. A. Cruz, and A. M. S. Mendes, "Multistage predictive current control based on virtual vectors for the reduction of current harmonics in six-phase PMSMs," *IEEE Trans. Energy Convers.*, vol. 36, no. 2, pp. 1368–1377, Jun. 2021.

[15] L. Huang, J. Ji, W. Zhao, T. Tao, and J. Cui, "Duty-ratio-based direct torque control with enhanced harmonic current suppression for dual-three-phase permanent magnet motor," *IEEE Trans. Power Electron.*, vol. 37, no. 9, pp. 11098–11108, Sep. 2022.

[16] P. Garcia-Entrambasaguas, I. Zoric, I. González-Prieto, M. J. Duran, and E. Levi, "Direct torque and predictive control strategies in nine-phase electric drives using virtual voltage vectors," *IEEE Trans. Power Electron.*, vol. 34, no. 12, pp. 12106–12119, Dec. 2019.

[17] H. Wang, X. Zheng, X. Yuan, and X. Wu, "Low-complexity model-predictive control for a nine-phase open-end winding PMSM with dead-time compensation," *IEEE Trans. Power Electron.*, vol. 37, no. 8, pp. 8895–8908, Aug. 2022.

[18] Y. Luo and C. Liu, "A flux constrained predictive control for a six-phase PMSM motor with lower complexity," *IEEE Trans. Ind. Electron.*, vol. 66, no. 7, pp. 5081–5093, Jul. 2019.

[19] Z. Zhou, C. Xia, Y. Yan, Z. Wang, and T. Shi, "Torque ripple minimization of predictive torque control for PMSM with extended control set," *IEEE Trans. Ind. Electron.*, vol. 64, no. 9, pp. 6930–6939, Sep. 2017.

[20] Y. Luo and C. Liu, "Elimination of harmonic currents using a reference voltage vector based-model predictive control for a six-phase PMSM motor," *IEEE Trans. Power Electron.*, vol. 34, no. 7, pp. 6960–6972, Jul. 2019.

[21] O. Gonzalez et al., "Model predictive current control of six-phase induction motor drives using virtual vectors and space vector modulation," *IEEE Trans. Power Electron.*, vol. 37, no. 7, pp. 7617–7628, Jul. 2022.

[22] X. Wu, W. Song, and C. Xue, "Low-complexity model predictive torque control method without weighting factor for five-phase PMSM based on hysteresis comparators," *IEEE J. Emerg. Sel. Topics Power Electron.*, vol. 6, no. 4, pp. 1650–1661, Dec. 2018.

[23] Y. Yang et al., "Low complexity finite-control-set MPC based on discrete space vector modulation for T-type three-phase three-level converters," *IEEE Trans. Power Electron.*, vol. 37, no. 1, pp. 392–403, Jan. 2022.

[24] Y. Luo and C. Liu, "A simplified model predictive control for a dual three-phase PMSM with reduced harmonic currents," *IEEE Trans. Ind. Electron.*, vol. 65, no. 11, pp. 9079–9089, Nov. 2018.

[25] T. Tao, W. Zhao, Y. Du, Y. Cheng, and J. Zhu, "Simplified fault-tolerant model predictive control for a five-phase permanent-magnet motor with reduced computation burden," *IEEE Trans. Power Electron.*, vol. 35, no. 4, pp. 3850–3858, Apr. 2020.

[26] Y. Yang, H. Wen, M. Fan, M. Xie, and R. Chen, "Fast finite-switching-state model predictive control method without weighting factors for T-type three-level three-phase inverters," *IEEE Trans. Ind. Inform.*, vol. 15, no. 3, pp. 1298–1310, Mar. 2019.

[27] S. Yan, Y. Cui, C. Li, X. Gao, and Y. Cai, "An improved FCS-MPC based on novel sector optimization and capacitor charge balance algorithm for T-type 3P-3L converters," *IEEE Trans. Power Electron.*, vol. 38, no. 4, pp. 4559–4571, Apr. 2023.

[28] T. Liu, A. Chen, and Y. Huang, "Multivector model predictive current control for paralleled three-level T-type inverters with circulating current elimination," *IEEE Trans. Ind. Electron.*, vol. 70, no. 8, pp. 8042–8052, Aug. 2023.

[29] Yongchang Zhang, W. Xie, Z. Li, and Y. Zhang, "Model predictive direct power control of a PWM rectifier with duty cycle optimization," *IEEE Trans. Power Electron.*, vol. 28, no. 11, pp. 5343–5351, Nov. 2013.

[30] M. Ayala, J. Doval-Gandoy, J. Rodas, O. Gonzalez, R. Gregor, and M. Rivera, "A novel modulated model predictive control applied to six-phase induction motor drives," *IEEE Trans. Ind. Electron.*, vol. 68, no. 5, pp. 3672–3682, May 2021.

[31] S.-W. Kang, J.-H. Soh, and R.-Y. Kim, "Symmetrical three-vector-based model predictive control with deadbeat solution for IPMSM in rotating reference frame," *IEEE Trans. Ind. Electron.*, vol. 67, no. 1, pp. 159–168, Jan. 2020.

[32] J. Ji, S. Jin, W. Zhao, D. Xu, L. Huang, and X. Qiu, "Simplified three-vector-based model predictive direct power control for dual three-phase PMSG," *IEEE Trans. Energy Convers.*, vol. 37, no. 2, pp. 1145–1155, Jun. 2022.

Jia Cui received the M.Sc. degree in control science and engineering from the Jiangsu University of Science and Technology, Zhenjiang, China, in 2019, and the Ph.D. degree in electrical engineering from Jiangsu University, Zhenjiang, China, in 2023.

He has been a Lecturer with the School of Automation, Jiangsu University of Science and Technology, since September 2023. His research interests include the design and control of electric machine and drive.

Tao Tao received the B.Sc. degree from Nanjing Agricultural University, Nanjing, China, in 2009, and the Ph.D. degree from Jiangsu University, Zhenjiang, China, in 2020, both in electrical engineering.

Since 2021, he has been with Jiangsu University, where he is currently a Lecturer with the School of Electrical Information Engineering. His research interest focuses on the control of multiphase permanent-magnet machines.

Wenxiang Zhao (Senior Member, IEEE) received the B.Sc. and M.Sc. degrees from Jiangsu University, Zhenjiang, China, in 1999 and 2003, respectively, and the Ph.D. degree from Southeast University, Nanjing, China, in 2010, all in electrical engineering.

From 2008 to 2009, he was a Research Assistant with the Department of Electrical and Electronic Engineering, University of Hong Kong, Hong Kong. From 2013 to 2014, he was a Visiting Professor with the Department of Electronic and Electrical Engineering, University of Sheffield, Sheffield, U.K. He is currently a Professor with the School of Electric Power Engineering, Nanjing Institute of Technology, Nanjing, China, and also with the School of Electrical and Information Engineering, Jiangsu University. He has authored and coauthored more than 150 papers published in various IEEE transactions. His current research interests include electric machines and control.